ADVANCED MATERIALS TECHNOLOGIES
www.advmattechnol.de

Efficient Large Area Semi-Transparent Dye-Sensitized Solar Cells (DSSCs) Printed with DMD400 Technology

Mahfoudh Raïssi, Himal Muwanwella, Falak Naz, Anaïs Bianchi, Didier Rousseau, and Muhammad Tariq Sajjad**

This work presents the development of fully printed, large-area, semi-transparent Dye-Sensitized Solar Cells (DSSCs) using TiO_2 nanoparticles treated with $TiCl_4$, a "D35" push-pull dye sensitizer, and I_3^-/I^- redox mediator. Cells with areas of 4 and 200 cm^2 were printed using hexagonal, stripe, and standard designs, employing digital materials deposition (DMD) technology. The porous films printed via DMD, confirmed by scanning electron microscopy (SEM), improved solar cells performance by enhancing the Open Circuit Voltage (Voc) and fill factor (FF). The hexagonal design, in particular, facilitated better electrolyte impregnation in the TiO_2 mesoporous structure, boosting current density. This design yielded a power conversion efficiency (PCE) of 7.05% for 4 cm^2 DSSCs, surpassing the stripe (5.50%) and standard (5.48%) designs. Its higher performance can be attributed to lower interfacial charge recombination rates and improvedcharge transfer and collection efficiency. Photophysical measurements indicated faster charge transfer rates in hexagonal cells ($\approx 1.3 \times 10^9 s^{-1}$) compared to the stripe ($9.8 \times 10^8\ s^{-1}$) and standard ($9.5 \times 10^8\ s^{-1}$) designs. Hence, our work highlights the potential of hexagonal design to improve both efficiency and transparency while reducing material consumption, offering a promising approach for manufacturing semi-transparent solar cells.

1. Introduction

Photovoltaics have emerged as a vital environmentally friendly solution to meet energy demands over the past few decades. Among these, DSSCs stand out as a promising concept due to their distinct advantages, including a shorter payback time and higher performance under low light conditions, particularly under artificial lighting.[1–3] Other benefits include good transparency, a wide range of color options, compatibility with flexible substrates, and lightweight characteristics. Additionally, the use of competitively cheap materials for fabrication, coupled with the low investment required for manufacturing and extended lifetime, further favors DSSC cells. These advantages make DSSC cells an attractive photovoltaic technology for outdoor applications such as Building Integrated Photovoltaic (BIPV) products,[4] flexible devices for walls or windows, and indoor applications like low-power wireless electronic devices.

The development of new sensitizers, particularly those incorporating non-noble elements,[5,6] and the discovery of new redox mediators,[7,8] which exhibit more positive redox potentials than iodide/triiodide, have led to an increase in the photovoltage and PCE of the cell. For the photoanode, TiO_2 nanomaterials, n-type semiconductor, are widely used due to their favorable band positions, high transparency,[8] high stability, and low cost.[9–12] TiO_2 mesoporous films with various morphologies, such as nanoparticles (NPs),[6,13] nanotubes,[14–17] and nanowires,[18–20] have been employed as the photoanode in DSSCs. Among these, TiO_2 NPs exhibit superior performance compared to others due to their ability to provide larger surface areas for light harvesting. However, the size of the TiO_2 NPs strongly influences the photovoltaic performances of DSSCs. Yanagida et al.[21] reported on the size dependence of electron diffusion and recombination processes in TiO_2 film, resulting in significant differences in charge collection properties. Cao et al.[22,23] found that larger TiO_2 NPs (32 nm) exhibit low electron transport resistance and high recombination resistance, leading to superior charge collection efficiency. However, increasing the size of TiO_2 NPs beyond a certain level is detrimental to the overall performance, mainly due to the reduction in available surface area for dye loading and light harvesting.

In addition to materials development, the deposition technique for TiO_2 nanomaterials is a key factor in improving overall performance. Screen printing is a widely used deposition technique in DSSCs compared to inkjet printing, spray coating, and

M. Raïssi, A. Bianchi, D. Rousseau
KELENN Technology
6 rue Ampère, Igny 91430, France
E-mail: mahfoudh.raissi@kelenntech.com
H. Muwanwella, F. Naz, M. T. Sajjad
School of Engineering
London South Bank University
103 Borough Road, London SE1 0AA, UK
E-mail: sajjadt@lsbu.ac.uk

The ORCID identification number(s) for the author(s) of this article can be found under https://doi.org/10.1002/admt.202400637

DOI: 10.1002/admt.202400637

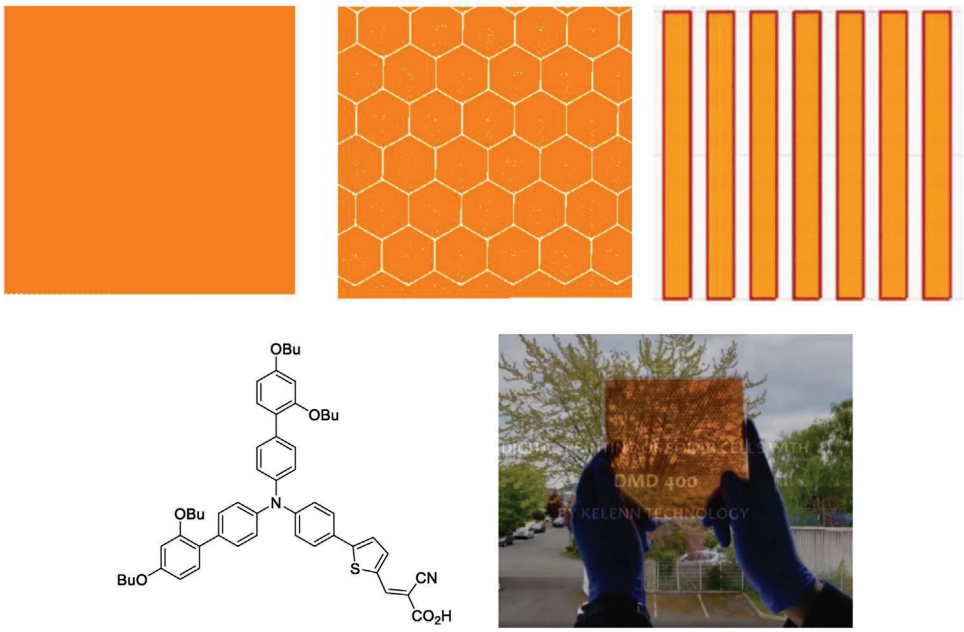

Figure 1. (Top) pictures of three printed solar cell designs: standard (left), hexagonal (middle), stripe (right). (Bottom) Structure of the D35 dye and picture of the 225 cm^2 DSSC prepared by KELENN digital printing technology.

doctor blade coating.[19,24] Gratzel et al. reported an efficiency of 14% for lab-scale cells.[9–11] and a PCE of 11% for a large area cell (22 cm^2) produced using screen printing.[13] These devices even demonstrated an efficiency of 10% under thermal stress at 85 °C[12] during 1000 h of light soaking with a liquid ionic-based electrolyte. Despite these advancements in this technology, the efficiency remains low compared to organic photovoltaics (OPVs) with non-fullerene acceptors (NFAs) and perovskite solar cells (PSCs).

The restructuring of TiO_2 photoanode can improve DSSC performance by enhancing dye loading, reducing defects, and decreasing the interfacial recombination rate. In response to this, KELENN Technology has recently developed a new printing technology named Digital Materials Deposition (DMD) with two sizes (DMD100 and DMD400). This technology allows the easy printing of a complete DSSC device with various designs by printing TiO_2 NPs paste, electrolyte, and dye. In this work, we fabricated solar cells with a surface area of 4 cm^2 using three DMD printed designs (**Figure 1**), employing the classical push-pull organic dye D35 and a liquid electrolyte based on iodide/triiodide redox mediator, and compared their performances. The J–V and IPCE measurements of the resulting cells showed that the hexagonal design outperformed the stripe and standard designs. This improvement is due to more efficient charge transfer and charge collection in cells with a hexagonal structure. Additionally, we used this new printing technology to quickly and efficiently print a large area (200 cm^2) DSSC.

2. Results and Discussion

The morphology of the TiO_2 photoanode with hexagonal geometry printed by DMD was investigated using optical microscopy, SEM, and TEM. **Figure 2**a displays the optical microscopy image of the TiO_2 hexagonal photoanode printed with DMD400. The inset white rectangle image shows the mechanical profilometer scan of the 5 patterns of TiO_2, confirming the homogeneity of thickness (thickness = 5 µm) and the step that separates the patterns (step = 150 µm). Figure 2b shows the plane view of SEM images of one TiO_2 pattern. The TiO_2 nanoparticles exhibit approximately spherical shapes and are randomly distributed. Interestingly, the TiO_2 film deposited by DMD seems to have slightly higher porosity, possibly due to the absence of mechanical/shear stress on the TiO_2 paste during the printing process. Figure 2c depicts the cross-sectional TEM images of the TiO_2 electrodes based on hexagonal geometry prepared by polishing with an Ar-ion beam, with a magnification of the top and bottom part of the layer. The nanocrystalline-printed TiO_2 layer appears very homogeneous, smooth, and flat. Also, the porosity of the electrode is completely homogeneous throughout the film. This large open hexagonal structure printed by DMD could increase the infiltration of the electrolyte compared to standard and stripe structures, thereby enhancing the photocurrent density.

The DSSCs fabricated with digital printing methods typically yield better performance than those produced with conventional screen-printing techniques, regardless of the surface area of the DSSCs.[24–27] This suggests that the design of the TiO_2 electrodes is important and can influence photovoltaic performance. We utilized digitally printed TiO_2 films to produce DSSCs with the D35 sensitizer and the classical iodide/triiodide redox mediator and compared their photovoltaic performances with DSSCs prepared with conventionally screen-printed TiO_2 nanoparticles. Typical current/voltage and IPCE spectra of 4 cm^2 cells are shown in **Figure 3**a,b, whereas the current/voltage of 200 cm^2 cells is given in Figure 3d. The metrics of the solar cells (average of ≈6 different cells) are gathered in **Table 1**.

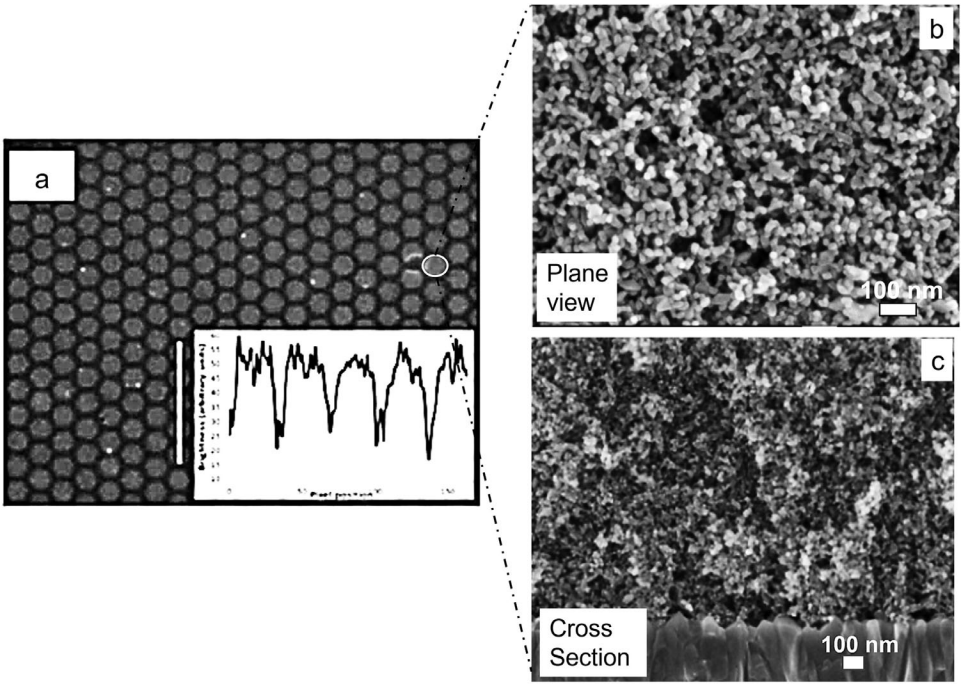

Figure 2. a) Plane view of the optical microscopy image of the TiO_2 photoanode, with the inset white rectangle displaying the profilometer scan of a small hexagonal surface. b) Plane view of the SEM image of a hexagonal geometry of the TiO_2 mesoporous layer printed using DMD technology. c) Cross-sectional TEM image of a TiO_2 hexagonal design printed using DMD technology.

Table 1 shows that the hexagonal design outperforms both the stripe and standard designs. The devices with a 4 cm^2 surface area demonstrate a high Voc (> 0.76 V), with current densities progressively increasing from 10.03 to 11.77 mA cm^{-2} across the standard, stripe, and hexagonal designs. The FF also improves, from 0.72 to 0.76, leading to an increase in PCE from 5.48% to 7.05%. The higher PCE observed in hexagonal photoanode-based cells is primarily due to enhanced charge collection efficiency, as confirmed by IMVS and IMPS measurements, and reduced charge recombination losses. This improvement is not due to higher light harvesting efficiency, as the amount of dye was slightly lower in the hexagonal structure compared to the standard (confirmed by adsorption experiments). The fractal surface of the hexagonal design enhances $TiCl_4$ treatment, reducing defect density in the TiO_2 mesoporous layer. This effective surface treatment improves defect passivation and facilitates better charge transfer by promoting electrolyte diffusion within the mesoporous layer.

Photovoltaic performance was notably higher for devices with a smaller surface area (4 cm^2), achieving approximately double the efficiency of larger devices (200 cm^2). This improvement can be attributed to the lower defect density in the smaller device, which reduces charge recombination and decreases charge transfer resistance. In contrast, devices with a larger area (200 cm^2) exhibit a higher defect density, leading to increased recombination, higher resistance, and reduced efficiency.

To assess transparency, the hexagonal 4 cm^2 devices were tested by illuminating both through the TiO_2 photoanode and the Pt counter electrode. Good transparency (T > 60%) was achieved, as shown by the transmittance spectrum in Figure S1 (Supporting Information), with an average PCE of 6.75% for TiO_2-side illumination and 6.25% for Pt counter electrode-side illumination across the measured 4 cells (Table S1 and Figure S2, Supporting Information). The hexagonal design enhanced the optical field distribution, improving light transmission through the TiO_2 photoanode and increasing dye absorption, which generated more charge carriers with lower recombination rates. $TiCl_4$ treatment of the TiO_2 photoanode further increased charge injection by reducing recombination. Additionally, the use of DMD technology to print the Pt counter electrode improved transparency while maintaining conductivity, thereby enhancing hole transport. As a result, the photovoltaic performance remained consistent, regardless of the side illuminated.

To investigate the effect of photoanode designs on the photocatalytic activity of DSSCs, we performed electrochemical impedance spectroscopy (EIS) using TiO_2 photoanodes with different designs (standard, stripe, and hexagonal), along with a Pt counter electrode and an electrolyte solution. This configuration allows us to assess both the electrochemical activity and photovoltaic performance (PCE) by taking into account the influence of the photoanode design.[31–39] The resultant EIS data are presented in a complex plane (Nyquist plot), where the imaginary impedance (Y-axis) represents the capacitive and inductive behavior of the DSSC, and the real impedance (X-axis) represents the resistive behavior.[36]

The Nyquist plot (Figure 3d) of a DSSC shows two semicircles: a smaller one at higher frequencies (100 Hz–1 MHz), corresponding to the charge-transfer resistance (R1) and capacitance (C1), attributed to processes at the electrolyte/Pt counter electrode interface; and a larger one at lower frequencies (0.1–100 Hz), corresponding to the recombination resistance (R2) and chemical capacitance (C2) across the TiO_2/dye/electrolyte

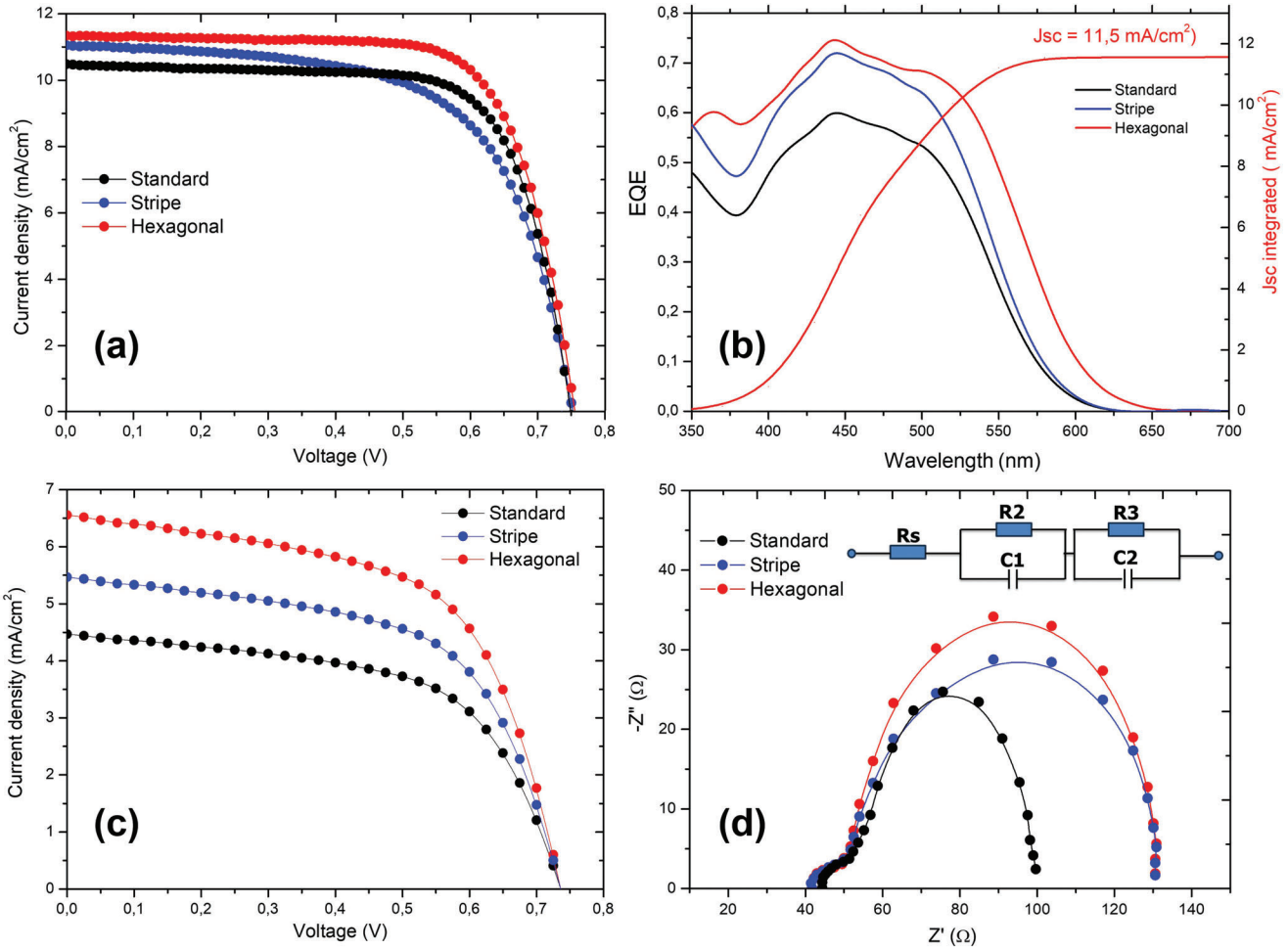

Figure 3. a) Current-voltage characteristics and b) EQE and integrated current of 4 cm^2 DSSCs printed using three designs (standard, stripe, and hexagonal) with DMD. c) Current-voltage characteristics of 200 cm^2 DSSCs. d) Nyquist plots for different photoanode designs (hexagonal, stripe, and standard); inset: the equivalent circuit model used for fitting.

interface.[31–39] The equivalent circuit, shown in the inset of Figure 3d, includes Rs, the series charge-transfer resistance at the FTO/TiO_2 contact. The impedance spectra were fitted to this equivalent circuit using Z-view software, and the fitted values are provided in **Table 2**.

The DSSC with a hexagonal design exhibits a higher recombination resistance (R2 = 171 Ω) and lower charge-transfer resistance (R1 = 9 Ω) compared to the standard design, which shows a lower recombination resistance (R2 = 74 Ω) and higher charge-transfer resistance (R1 = 17 Ω). The higher recombination resistance in the hexagonal design indicates a longer electron lifetime, implying a slower electron recombination process between the injected electrons and the I_3^- ions in the electrolyte. This finding highlights the impact of the fractal TiO_2 surface in the hexagonal design on enhancing short-circuit current densities and efficiencies (PCE), as reflected in the photovoltaics values.

Table 1. Photovoltaic performance parameters of standard, stripe, and hexagonal design-based solar cells fabricated using digital printing with D35 as the sensitizer, illuminated with a calibrated AM1.5 solar simulator (100 mW cm^{-2}).

DSSC designs	TiO_2 mp	Surface area [cm^2]	Jsc [mA cm^{-2}]	Voc [mV]	FF [%]	PCE [%]
Standard	Without scattering layer	4	10.03 (±0.21)	760 (±5)	72 (±1)	5.48 (±0.15)
		200	4.50 (±0.1)	740 (±10)	64 (±1)	1.95 (±0.05)
Stripe	Without scattering layer	4	11.15 (±0.20)	760 (±5)	65 (±1)	5.50 (±0.15)
		200	5.50 (±0.10)	740 (±2)	64 (±1)	2.60 (± 0.15)
hexagonal	Without scattering layer	4	11.77 (±0.10)	770 (±2)	76 (±1)	7.05 (± 0.15)
		200	6.60 (±0.10)	740 (±2)	68 (±1)	3.40 (± 0.15)

Table 2. Fitted resistance values of Rs, R1, and R2 were used for all three designs.

Design	R1: Transfer charge resistance [Ω]	R2: Recombination resistance [Ω]
Standard	17.32	74
Stripe	12.22	145
Hexagonal	9.45	171

The use of the hexagonal structure can improve electron diffusion and minimize charge recombination within DSSC devices. To investigate this, we employed IMPS and IMVS measurements to study the dynamics of electron transport, charge recombination, diffusion length, and charge collection efficiency (raw data provided in Figure S3, Supporting Information). **Figure 4a** shows that electron transport time (τ_d) decreases across all three structures as light intensity increases, thereby improving the electron diffusion coefficient (D_n), particularly in the hexagonal and stripe devices, as illustrated in Figure 4b. This suggests that electron diffusion is more efficient in the TiO_2 mesoporous layer with hexagonal and stripe structures under higher light intensities.[15] Furthermore, the hexagonal structure demonstrated a shorter τ_d and a larger D_n compared to the standard and stripe structures, indicating faster electron transport in the TiO_2 photoelectrode with a hexagonal structure. This can be attributed to the effectiveness of $TiCl_4$ treatment on the hexagonal structure, which enabled better passivation of the traps and the defects. As a result, the trapping/de-trapping process of photogenerated electrons in the TiO_2 mesoporous layer under the hexagonal structure is inhibited, promoting rapid electron transport.

The electron lifetime (τ_n), representing the time taken by an electron in TiO_2 mesoporous nanoparticle films to recombine with hole/electron acceptor at the TiO_2 and electrolyte interface,[16] is depicted in Figure 4c. The electron lifetime (τ_n), which is crucial for efficient charge collection, showed a similar trend in all three structures as the light intensity increased. This behavior is due to the high porosity of the TiO_2 layer printed using the DMD technique and the effective $TiCl_4$ treatment. These factors improved the coverage of the D35 dye on the TiO_2 surface, leading to increased interfacial recombination resistance and reduced trap states in TiO_2. This suppresses geminate recombination by preventing the back reaction of the injected electron in the electrolyte.[16,25–27]

The average electron diffusion length (L_n) and charge collection efficiency ($\eta_{collect}$) were calculated using Equations (4) and (5). Analysis of these parameters, plotted in Figure 4d,e as a function of light intensity, reveals that the higher Jsc, Voc, and FF in solar cells with a hexagonal structure are primarily due to enhanced diffusion length and charge collection efficiency, resulting from a prolonged electron lifetime and faster electron transport. Therefore, the superior performance of the hexagonal structure can be attributed to the high porosity of the TiO_2 photoelectrode, which facilitates electrolyte infiltration into the structure. Additionally, improved passivation of defects likely contributes to better electron transport and collection, leading to increased current density, Voc, and FF.

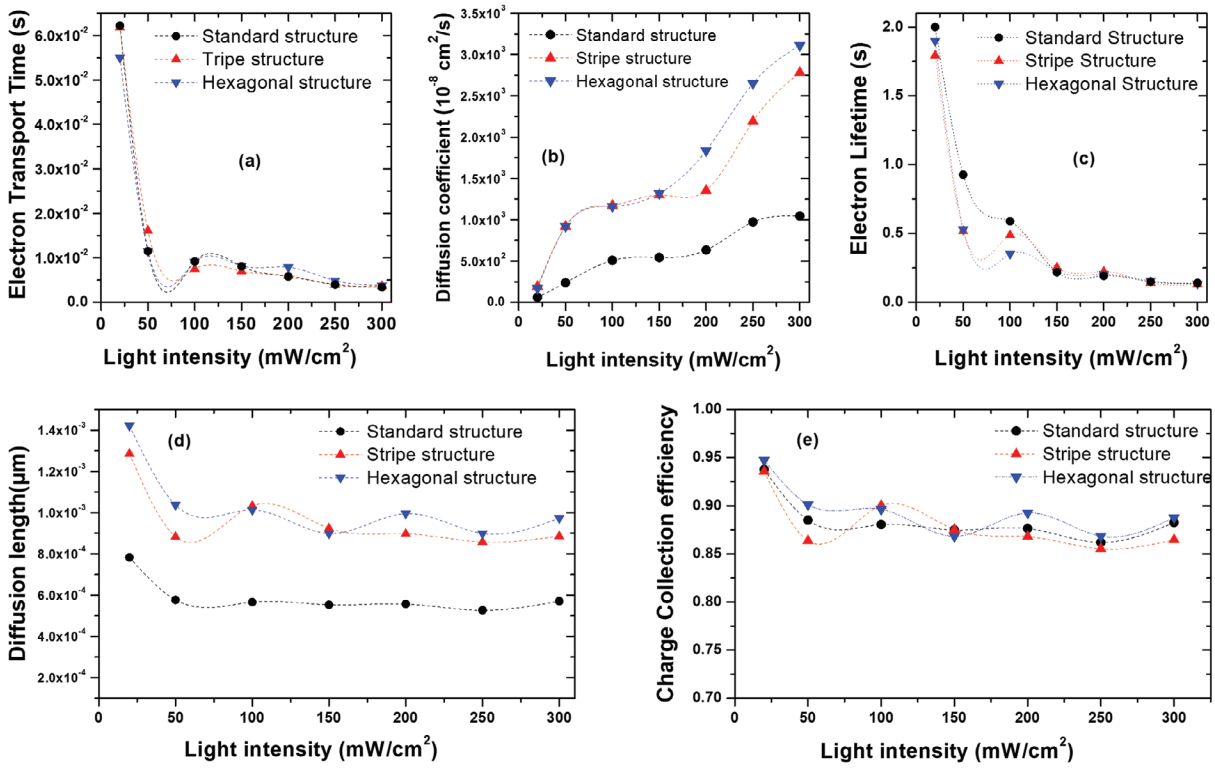

Figure 4. a) Electron transport time, b) diffusion coefficient, c) electron lifetime, d) diffusion length, e) charge collection efficiency, all versus incident light intensity.

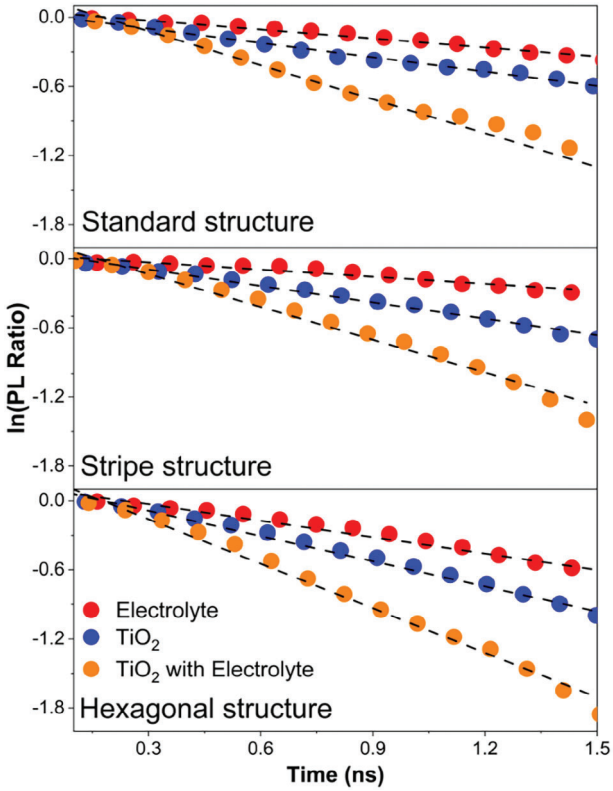

Figure 5. Natural logarithms of the ratio of the PL of dye D35 with the quencher (TiO_2, electrolyte, or both) and the PL of dye D35 on Al_2O_3. Dotted lines represent slopes, which are equivalent to the rate of quenching.

To understand how different designs influence the charge carrier dynamics, we performed time-resolved spectroscopy. We first measured the photoluminescence (PL) decay of sensitizer D35 on Al_2O_3 (Figure S4, Supporting Information) and used it as a reference. Al_2O_3 was used between the dye and glass to prevent possible quenching from the glass surface. Since Al_2O_3 has a very wide bandgap (7.0 eV),[30] the PL decay of sensitizer D35 on the Al_2O_3 provided the actual lifetime of D35. Remarkably, the dye D35 exhibited a similar lifetime ($T_{1/e} = \approx 1.1$ ns) for all three structures (standard, stripe, and Hexagonal). This suggests that the adsorber structure alone does not affect the functionality of the absorber. For assessing charge transfer rates, PL decays of dye with either electrolyte, TiO_2, or both (TiO_2 and electrolyte) were measured (Figure S4, Supporting Information). The PL decay of dye with electrolyte was used to extract the hole transfer rate, while the electron transfer rates were extracted from the decay of dye on the TiO_2 adsorber without the electrolyte. Moreover, the overall charge transfer rates were determined from dye adsorbed on TiO_2 immersed in the electrolyte.

For quantitative analysis, we took the natural logarithm of the ratio of the decay of D35 with the quencher (TiO_2 or electrolyte) to the decay of Al_2O_3 (**Figure 5**). The absolute value of the gradient represents how fast the charges are transferred to the transport layers. We determined these transfer rates from the slopes of these graphs.[28,29]

$$k_{et}(t) = -\frac{d}{dt}\left(\ln\left(\frac{\text{Absorber on the } TiO_2/\text{Electrolyte}}{\text{Absorber on } Al_2O_3}\right)\right) \quad (1)$$

Table 3. Charge transfer rates of standard, stripe, and hexagonal structures.

	Standard K_{CT} [$\times 10^8$ s^{-1}]	Stripe K_{CT} [$\times 10^8$ s^{-1}]	Hexagonal K_{CT} [$\times 10^8$ s^{-1}]
Electrolyte	2.0 ± 0.2	2.5 ± 0.3	4.8 ± 0.5
TiO_2	4.7 ± 0.5	4.1 ± 0.4	7.2 ± 0.7
TiO_2 with Electrolyte	9.5 ± 0.9	9.8 ± 0.9	12.8 ± 1.2

The resulting transfer rates for all three structures are provided in **Table 3**. The charge transfer rates range from 2×10^8 s^{-1} to 1.3×10^9 s^{-1}, indicating that charge transfer in all systems is rapid. Overall, the hexagonal structure exhibited the highest electron transfer, hole transfer, and overall charge transfer.

The higher charge transfer rates observed in the hexagonal system are attributed to the enhanced effective surface area of the structures, which provide more percolation pathways for the electrolyte and improve charge extraction upon excitation. This enhancement is reflected in the device data, particularly evident in the J–V curves where decreased series resistance and increased Jsc have been observed in the stripe and hexagonal structures, indicating improved charge extraction in these modified systems. The photophysical analysis suggests that this improvement stems from the increase in percolation pathways due to structural modifications.

To determine whether enhanced light harvesting and device performance in the hexagonal structure is due to increased dye loading, we conducted desorption experiments (Figure S5, Supporting Information). The dye concentration for standard, hexagonal, and stripe structures on 4 cm^2 areas were 4.32 10^{-6}, 4.05 10^{-6}, and 3.78 10^{-6} mol cm^{-2}, respectively. Although the standard structure exhibited slightly higher dye loading, the hexagonal structure outperformed it in photovoltaic efficiency. This suggests that improved performance in the hexagonal structure is due to better charge transfer and collection, as confirmed by photophysical data and IMVS/IMPS measurements. These findings highlight the importance of the TiO_2 electrode structure in enhancing the photovoltaic performance of DSSCs.

3. Conclusion

In summary, we printed semi-transparent DSSCs with standard, stripe, and hexagonal structures using the same printing process on 4 and 200 cm^2 surface areas. We observed better photovoltaic performance on the hexagonal structure compared to the stripe and standard structures. This improvement can be attributed to the favorable porosity of the film with the hexagonal geometry, printed with DMD technology, which enhances the impregnation of the dye and the electrolyte into the mesoporous TiO_2 structure. These enhancements lead to increased photovoltaic performance by improving Voc, FF, and current density. Hence, our study demonstrates that this new design of printed photoanode improves both the efficiency and transparency of DSSC devices. Additionally, the printed hexagonal structure reduces material consumption, featuring an innovative and attractive design for manufacturing efficient and semi-transparent DSSCs, OPVs, and PSCs.

4. Experimental Section

Device Fabrication and Characterization: The FTO-coated glass substrates were purchased from TEC15 and TEC7, with sheet resistances of 15 and 7 Ω sq^{-1}, respectively. They were used as the substrates for the photoanodes and counter electrodes, respectively. The substrates were first ultrasonically cleaned in acetone, water with detergent, and isopropanol for 30 min each. Subsequently, the substrates were sintered at 500 °C for 30 min. All films were printed with DMD100 and DMD400 printing technology [patent: FR1854610-2018]. The process began with the printing of a diluted solution in ethanol (75 wt.%) of the TiO_2 blocking layer at 40 °C on cleaned FTO using a slot-die printing head at a printing speed of 5 mm $^{-1}$s. Then, TiO_2 pastes (P25) with average particle sizes of ≈20 nm were printed with a needle printing head at 50KPA of printing pressure with a printing speed of 1000 mm min^{-1} to obtain a transparent nanocrystalline mesoporous layer with a thickness of ≈10 µm and an area of 4 and 200 cm^2.

The photoanodes were sintered at 500 °C for 30 min to remove the additives such as ethyl cellulose and terpineol in the pastes. After sintering, the TiO_2 films were treated with a 40 mM $TiCl_4$ aqueous solution at 70 °C for 30 min within the DMD printer, then rinsed with water, ethanol, and sintered again. This process healed the defects and increased the contact between the TiO_2 nanoparticles. The D35 dye (2 mg mL^{-1} in ethanol) was loaded onto TiO_2 photoanodes with very low slot-die printing speed (20 mm min^{-1}) for 5 min, and then washed with ethanol to remove the excess. The platinized counter electrode was produced using the DMD printing process. The TiO_2 photoanodes were assembled with the counter electrode using a hot melt surlyn film. The redox electrolyte, composed of 30 mM I_2, 50 mM Lithium Iodide (LiI), 0.5M 4-tertbutyl pyridine, and 0.6 M N-propyl-N′-ethyl-methylimidazolium iodide in acetonitrile for the I_3^-/I^- electrolyte, was introduced through a hole drilled in the back of the counter electrode. Finally, the hole was sealed with surlyn film.

The thickness and morphologies of the TiO_2 film and sizes of TiO_2 NPs were characterized using a scanning electron microscope (SEM) and transmission electron microscope (TEM). The absorption and desorption of the dye were analyzed using a UV–visible absorption spectrometer.

The current-voltage characteristics of the device were determined by applying an external potential bias to the cell and measuring the photocurrent using a Keithley model 2400 digital source meter. A solar simulator, Oriel Lamp calibrated at 100 mW cm^{-2}, along with a Si reference solar cell, was used to determine the input optical power. The overall PCE of the photovoltaic cell was calculated from the integral photocurrent density (Jsc), the open circuit photovoltage (Voc), the fill factor of the cell (FF), and input power. The intensity of the IPCE data was collected in the wavelength range of 350–800 nm.

Intensity-Modulated Photocurrent Spectroscopy (IMPS) and Intensity-Modulated Photovoltage Spectroscopy (IMVS): Electron transport time and electron lifetimes or recombination were measured by IMPS and IMVS, respectively. IMPS and IMVS responses were measured at different bias light intensities of 20, 50, 100, 150, 200, 250, and 300 W m^{-2}. The electron diffusion coefficient (Dn) within TiO_2 film and the electron transport time (τ_d), the time for an injected electron to increase the current density through a TiO_2 film, were determined from the IMPS measurements using the following Equations (1) and (2):

$$\tau_d = \frac{1}{2} \times \pi \times f_{\min}\,(IMPS) \tag{2}$$

$$D_n = L^2 / 2.5\,\tau_d \tag{3}$$

where $f_{\min}(IMPS)$ is the characteristic frequency at the minimum of the imaginary component, and L is the thickness of the TiO_2 film, which is ≈3 µm for all TiO_2 films in this work. Additional information such as the electron lifetime (τ_{e-}) and electron diffusion length (L_n) in the TiO_2 photoanode, and charge collection rate (η_{cc}) could be obtained according to the following Equations (3–5).

$$\tau_n = \frac{1}{2} \times \pi \times f_{\min}\,(IMVS) \tag{4}$$

$$L_n = \sqrt{D_n\,\tau_{e-}}\;\;(IMVS) \tag{5}$$

$$\eta_{\text{collect}} = (1 - \tau_d / \tau_{e-}) \tag{6}$$

Photophysical Analysis of the Photoanode: The time-resolved photoluminescence (TRPL) spectroscopy was performed using an Edinburgh FLS1000 spectrometer equipped with a picosecond laser with an excitation source of 375 nm and Visible 980 PMT. To evaluate the lifetimes of the D35 dye, a wide-bandgap material Al_2O_3 (as an inert adsorber) was used between the dye and glass, whereas for charge transfer studies, TiO_2 (as an electron extractor) and an iodine-based electrolyte (as a hole extraction agent) were used. Three fully printed structures; standard, stripe, and hexagonal, were analyzed. Six samples, two from each structure with TiO_2 and Al_2O_3 were immersed in a D35 absorber solution (2 mg mL^{-1} diluted with ethanol) for 12 h and then washed with copious amounts of ethanol to remove un-adsorbed dye from the structures. Subsequently, the samples were tested with and without electrolyte, and PL decays were measured. During the measurement, the excitation beam was carefully focused on the structures.

Adsorption Measurement: The dyed electrodes with standard, stripe, and hexagonal structures were soaked for a few minutes in ≈1 mL of a solution containing 0.1 M $(CH_3)_4NOH$ in acetonitrile. They were then rinsed with the same solution until reaching a precise volume of 2 mL. Subsequently, the UV–vis absorption spectra of the three solutions were measured (Figure S5, Supporting Information), and the dye loading was estimated from the absorbance. For the calculation, an average of three independent measurements were used.[22]

Supporting Information

Supporting Information is available from the Wiley Online Library or from the author.

Acknowledgements

The authors gratefully acknowledge the collaboration with CEA-SEPIA and the financial support provided through the ANR/PIA4 recovery plan. H.M., F.N., and M.T.S. are thankful to the British Council and London South Bank University for their financial support. Moreover, the authors extend their appreciation for the collaboration between KELENN Technology, France, and the School of Engineering at London South Bank University, UK.

Conflict of Interest

The authors declare no conflict of interest.

Data Availability Statement

The data that support the findings of this study are available from the corresponding author upon reasonable request.

Keywords

charge transfer and collection, diffusion length, hexagonal structure, printed photoanode, screen printing

Received: April 22, 2024
Revised: September 24, 2024
Published online:

[1] B. O'Regan, M. Grätzel, *Nature* **1991**,*353*, 737.
[2] A. Hagfeldt, G. Boschloo, L. Sun, L. Kloo, H. Pettersson, *Chem. Rev.* **2010**, *110*, 6595.
[3] L. M. Gonçalves, V. de Zea Bermudez, H. A. Ribeiro, A. M. Mendes, *Energy Environ. Sci.* **2008**, *1*, 655.
[4] M. Freitag, J. Teuscher, Y. Saygili, X. Zhang, F. Giordano, P. Liska, J. Hua, S. M. Zakeeruddin, J. E. Moser, M. Grätzel, A. Hagfeldt, *Nat. Photonics* **2017**, *11*, 372.
[5] A. Mishra, M. K. R. Fischer, P. Bäuerle, *Angew. Chem., Int. Ed.* **2009**, *48*, 2474.
[6] Y. Ooyama, Y. Harima, *ChemPhysChem* **2012**, *13*, 4032.
[7] a) M. Wang, C. Grätzel, S. M. Zakeeruddin, M. Grätzel, *Energy Environ. Sci.* **2012**, *5*, 9394; b) B. Pashaei, H. Shahroosvand, P. Abbasi, *RSC Adv.* **2015**, *5*, 94814
[8] T. Baron, W. Naim, I. Nikolinakos, B. Andrin, Y. Pellegrin, D. Jacquemin, S. Haacke, F. Sauvage, F. Odobel, *Angewandte Chemie International 61*, **2022**, 202207459.
[9] S. Mathew, A. Yella, P. Gao, R. Humphry-Baker, B. F. E. Curchod, N. Ashari-Astani, I. Tavernelli, U. Rothlisberger, M. K. Nazeeruddin, M. Grätzel, *Nat. Chem.* **2014**, *6*, 242.
[10] A. Yella, H. W. Lee, H. N. Tsao, C. Yi, A. K. Chandiran, M. K. Nazeeruddin, E. W.-G. Diau, C. Y. Yeh, S. M. Zakeeruddin, M. Grätzel, *Science* **2011**, *334*, 629.
[11] K. Kakiage, Y. Aoyama, T. Yano, K. Oya, J.-i. Fujisawa, M. Hanaya, *Chem. Commun.* **2015**, *51*, 15894.
[12] P. Wang, L. Yang, H. Wu, Y. Cao, J. Zhang, N. Xu, S. Chen, J. D. Decoppet, S. M. Zakeeruddin, M. Grätzel, *Joule* **2018**, *2*, 2145.
[13] A. Fakharuddin, R. Jose, T. M. Brown, F. Fabregat-Santiago, J. Bisquert, *Energy Environ. Sci.* **2014**, *7*, 3952.
[14] M. Saifullah, J. Gwak, J. H. Yun, *J. Mater. Chem. A* **2016**, *4*, 8512.
[15] S. H. Kang, S. H. Choi, M. S. Kang, J. Y. Kim, H. S. Kim, T. Hyeon, Y. E. Sung, *Adv. Mater.* **2008**, *20*, 54.
[16] G. K. Mor, K. Shankar, M. Paulose, O. K. Varghese, C. A. Grimes, *Nano Lett.* **2006**, *6*, 215.
[17] M. Adachi, Y. Murata, J. Takao, J. Jiu, M. Sakamoto, F. Wang, *J. Am. Chem. Soc.* **2004**, *126*, 14943.
[18] S. G. Hashmi, M. Özkan, J. Halme, S. M. Zakeeruddin, J. Paltakari, M. Grätzel, P. D. Lund, *Energy Environ. Sci.* **2016**, *9*, 2453.
[19] Y. Kunugi, Y. Shimoyama, S. Umezu, *J. Photopolym. Sci. Tec.* **2013**, *26*, 383.
[20] S. G. Hashmi, M. Ozkan, J. Halme, K. D. Misic, S. M. Zakeeruddin, J. Paltakari, M. Grätzel, P. D. Lund, *Nano Energy* **2015**, *17*, 206.
[21] a) M. Özkan, S. G. Hashmi, J. Halme, A. Karakoç, T. Sarikka, J. Paltakari, P. D. Lund, *Org. Electron.* **2017**, *44*, 159; b) S. Nakade, Y. Saito, W. Kubo, T. Kitamura, Y. Wada, S. Yanagida, *J. Phys. Chem. B* **2003**, *107*, 8607.
[22] M. Raïssi, Y. Pellegrin, F. X. Lefevre, M. Boujtita, D. Rousseau, T. Berthelot, *Solar Energy* **2020**, *199*, 92.
[23] D. Cao, H. Yin, X. Yu, J. Zhang, Y. Jiao, W. Zheng, B. Mi, Z. Gao, *Adv. Eng. Mater.* **2019**, *22*, 1901071.
[24] H. G. Han, H. C. Weerasinghe, K. M. Kim, J. S. Kim, Y. B. Cheng, D. J. Jones, A. B. Holmes, T. H. Kwon, *Sci. Rep.* **2015**, *5*, 14645.
[25] D. P. Hagberg, X. Jiang, E. Gabrielsson, M. Linder, T. Marinado, T. Brinck, A. Hagfeldt, L. Sun, *J. Mater. Chem.* **2009**, *19*, 7232.
[26] X. Jiang, K. M. Karlsson, E. Gabrielsson, E. M. J. Johansson, M. Quintana, M. Karlsson, L. Sun, G. Boschloo, A. Hagfeldt, *Adv. Funct. Mater.* **2011**, *21*, 2944.
[27] X. Jiang, T. Marinado, E. Gabrielsson, D. P. Hagberg, L. Sun, A. Hagfeldt, *J. Phys. Chem. C* **2010**, *114*, 2799.
[28] J. P. abc, M. T. S. d, P.-H. Jouneau, A. R. d, J. F.-V. abc, I. D. W. Samuel, P. R. abc, D. Aldakov, *J. Mater. Chem. A* **2016**, *4*, 827.
[29] M. Raissi, M. T. Sajjad, Y. Pellegrin, T. J. Roland, S. Jobic, M. Boujtita, A. Ruseckas, D. W. Samuel, F. Odobel, *Nanoscale* **2017**, *9*, 15566.
[30] E. O. Filatova, A. S. Konashuk, *J. Phys. Chem. C* **2015**, *119*, 20755.
[31] A. Hauch, A. Georg, *Electrochim. Acta* **2001**, *46*, 3457.
[32] V. H. Pham, T. V. Cuong, S. H. Hur, E. W. Shin, J. S. Kim, J. S. Chung, E. J. Kim, *Carbon* **2010**, *48*, 1945.
[33] L. Kavan, J. H. Yum, M. Graetzel, *Electrochim. Acta* **2014**, *128*, 349.
[34] L. Kavan, J. H. Yum, M. Grätzel, *Nano Lett.* **2011**, *11*, 5501.
[35] L. Kavan, *Top. Curr. Chem.* **2014**, *348*, 53.
[36] F. Fabregat-Santiago, J. Bisquert, E. Palomares, L. Otero, D. Kuang, S. M. Zakeeruddin, M. Grätzel, *J. Phys. Chem. C* **2007**, *111*, 6550.
[37] S. Sarker, A. Ahammad, H. W. Seo, D. M. Kim, *Int. j. photoenergy* **2014**, *2014*, 851705.
[38] Q. Wang, J. E. Moser, M. Grätzel, *J. Phys. Chem. B* **2005**, *109*, 14945.
[39] L. Kavan, J. H. Yum, M. K. Nazeeruddin, M. Grätzel, *ACS Nano* **2011**, *5*, 9171.
[40] J. Yang, C. Bao, K. Zhu, T. Yu, F. Li, J. Liu, Z. Li, Z. Zou, *Chem. Commun.* **2014**, *50*, 4824.